



HAL
open science

MUSE Spectroscopic Identifications of Ultra-faint Emission Line Galaxies with $M_{UV} \sim -15$

Michael V Maseda, Roland Bacon, Marijn Franx, Jarle Brinchmann, Joop Schaye, Leindert Boogaard, Nicolas Bouche, Rychard J Bouwens, Sebastiano Cantalupo, Thierry Contini, et al.

► **To cite this version:**

Michael V Maseda, Roland Bacon, Marijn Franx, Jarle Brinchmann, Joop Schaye, et al.. MUSE Spectroscopic Identifications of Ultra-faint Emission Line Galaxies with $M_{UV} \sim -15$. The Astrophysical journal letters, 2018, 865 (1), pp.L1. 10.3847/2041-8213/aade4b . hal-02325247

HAL Id: hal-02325247

<https://hal.science/hal-02325247>
















Submitted on 22 Oct 2019

HAL is a multi-disciplinary open access archive for the deposit and dissemination of scientific research documents, whether they are published or not. The documents may come from teaching and research institutions in France or abroad, or from public or private research centers.

L'archive ouverte pluridisciplinaire **HAL**, est destinée au dépôt et à la diffusion de documents scientifiques de niveau recherche, publiés ou non, émanant des établissements d'enseignement et de recherche français ou étrangers, des laboratoires publics ou privés.



MUSE Spectroscopic Identifications of Ultra-faint Emission Line Galaxies with $M_{UV} \sim -15^*$

Michael V. Maseda^{1,10} , Roland Bacon², Marijn Franx¹ , Jarle Brinchmann^{1,3} , Joop Schaye¹ , Leindert A. Boogaard¹ ,
Nicolas Bouche^{4,2} , Rychard J. Bouwens¹ , Sebastiano Cantalupo⁵, Thierry Contini⁴ , Takuya Hashimoto^{6,7} , Hanae Inami²,
Raffaella A. Marino⁵ , Sowgat Muzahid¹ , Themiya Nanayakkara¹ , Johan Richard² , Kasper B. Schmidt⁸ ,
Anne Verhamme⁹ , and Lutz Wisotzki⁸

¹ Leiden Observatory, Leiden University, P.O. Box 9513, 2300 RA, Leiden, The Netherlands; maseda@strw.leidenuniv.nl

² Univ Lyon, Univ Lyon1, Ens de Lyon, CNRS, Centre de Recherche Astrophysique de Lyon UMR5574, F-69230, Saint-Genis-Laval, France

³ Instituto de Astrofísica e Ciências do Espaço, Universidade do Porto, CAUP, Rua das Estrelas, PT4150-762 Porto, Portugal

⁴ Institut de Recherche en Astrophysique et Planétologie (IRAP), Université de Toulouse, CNRS, UPS, F-31400 Toulouse, France

⁵ ETH Zürich, Department of Physics, Wolfgang-Pauli-Str. 27, 8093 Zürich, Switzerland

⁶ Department of Environmental Science and Technology, Faculty of Design Technology, Osaka Sangyo University, 3-1-1, Nagaito, Daito, Osaka 574-8530, Japan

⁷ National Astronomical Observatory of Japan, 2-21-1 Osawa, Mitaka, Tokyo 181-8588, Japan

⁸ Leibniz-Institut für Astrophysik Potsdam (AIP), An der Sternwarte 16, D-14482 Potsdam, Germany

⁹ Observatoire de Genève, Université de Genève, 51 Ch. des Maillettes, 1290 Versoix, Switzerland

Received 2018 July 24; revised 2018 August 17; accepted 2018 August 29; published 2018 September 14

Abstract

Using an ultra-deep blind survey with the MUSE integral field spectrograph on the European Southern Observatory Very Large Telescope, we obtain spectroscopic redshifts to a depth never before explored: galaxies with observed magnitudes $m_{AB} \gtrsim 30$ –32. Specifically, we detect objects via Ly α emission at $2.9 < z < 6.7$ without individual continuum counterparts in areas covered by the deepest optical/near-infrared imaging taken by the *Hubble Space Telescope*, the Hubble Ultra Deep Field. In total, we find 102 such objects in 9 square arcminutes at these redshifts. Detailed stacking analyses confirm the Ly α emission as well as the 1216 Å breaks and faint ultraviolet continua ($M_{UV} \sim -15$). This makes them the faintest spectroscopically confirmed objects at these redshifts, similar to the sources believed to reionize the universe. A simple model for the expected fraction of detected/undetected Ly α emitters as a function of luminosity is consistent with these objects being the high-equivalent width tail of the normal Ly α -emitter population at these redshifts.

Key words: galaxies: evolution – galaxies: high-redshift – quasars: emission lines

Supporting material: machine-readable table

1. Introduction

Traditional spectroscopic studies rely on a pre-selection of objects, typically via photometry. Objects are selected based on a variety of criteria and are then targeted with slits or fibers that feed into a spectrograph. While this technique is widely used, it is nevertheless unreliable for obtaining complete spectroscopic samples whenever the input photometric catalog is incomplete; e.g., when the objects of interest are near the detection limit of the imaging. This is particularly true when an emission line is the most significant contribution to the observed broadband magnitude, so objects with spectroscopically detectable emission lines with high equivalent widths (EWs) might not be present in photometric catalogs (e.g., Figure 7 of Maseda et al. 2018).

Pure blind spectroscopic studies require exquisitely well-understood data to ensure reliable line detections and data from the Multi-Unit Spectroscopic Explorer (MUSE; Bacon et al. 2010), an integral field spectrograph at the Very Large Telescope, are now in such a state. The recent survey of the Ultra Deep Field (UDF) with MUSE (Bacon et al. 2017, hereafter B17) reaches an unprecedented spectroscopic depth

($< 3 \times 10^{-19}$ erg s $^{-1}$ cm $^{-2}$ at 7000 Å; 3- σ for a spatially and spectrally unresolved line).

One result from B17, which is also hinted at in Bacon et al. (2015), is the presence of numerous emission line sources with no counterpart in catalogs based on *Hubble Space Telescope* (HST) imaging. While a fraction of these sources are not in photometric catalogs due to close blending issues, the remainder are plausibly extremely faint in the continuum ($m_{AB} \gtrsim 30$). They are believed to be H I Ly α emitters (LAEs) at redshifts $2.9 < z < 6.7$ due to an asymmetric line profile and/or the lack of other spectral features that would be indicative of lower- z sources. The implied ultraviolet (UV) magnitudes ($M_{UV} > -16$) are intriguing as galaxies this faint are thought to have reionized the universe at $z > 6$, but have so far remained elusive spectroscopically (e.g., Bouwens et al. 2012; Finkelstein et al. 2012). Detections of the UV continuum or other spectral features would provide further evidence that these “invisible” galaxies are indeed high- z LAEs.

In practice, deep non-detections of the UV continuum of an LAE implies that Ly α has a large EW. The interest in these LAEs is due to theoretical expectations where $EW_{Ly\alpha} \lesssim 200$ Å if the photons are produced by normal stellar populations (Charlot & Fall 1993). This value can be exceeded at extremely low metallicities ($\lesssim 1\% Z_{\odot}$), young ages ($\lesssim 10$ Myr), or with non-standard stellar initial mass functions, which are potential signatures of the earliest populations of galaxies in the universe (Schaerer 2003; Raiter et al. 2010; and also the discussion in

* Based on observations made with ESO telescopes at the La Silla Paranal Observatory under program IDs 094.A-2089(B), 095.A-0010(A), 096.A-0045(A), and 096.A-0045(B); and based on data obtained with the NASA/ESA *Hubble Space Telescope*, which is operated by the Association of Universities for Research in Astronomy, Inc., under NASA contract NAS 5-26555.

¹⁰ NOVA Fellow.

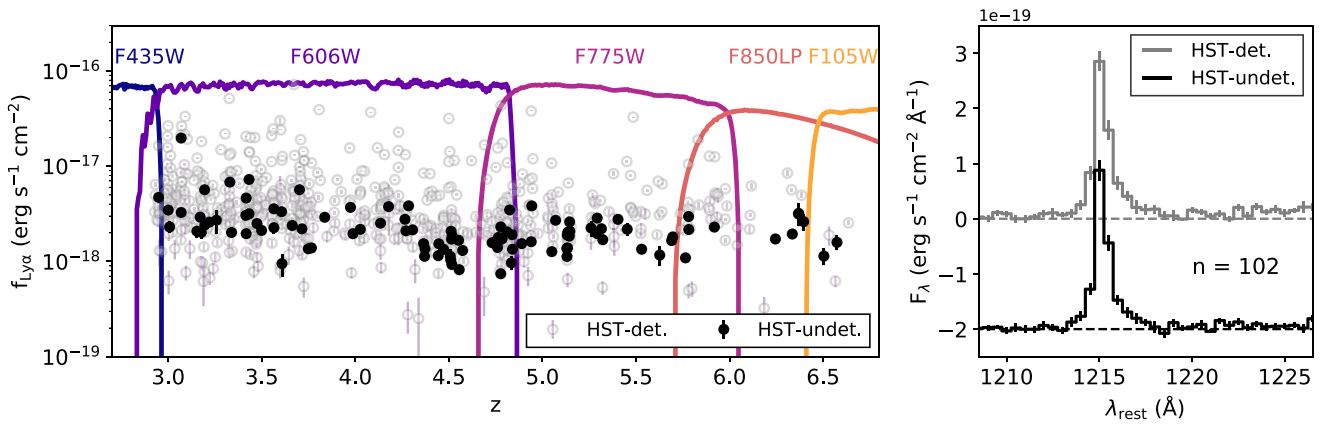


Figure 1. Left panel: $f_{\text{Ly}\alpha}$ vs. z for the *HST*-undetected (filled circles) and *HST*-detected MUSE LAEs (open circles), with *HST* imaging filter curves denoted by solid lines. Right panel: MUSE spectral stacks (median; bootstrap uncertainties) of LAEs. The black spectrum shows the *HST*-undetected LAEs (offset by -2) and the gray spectrum is a flux- and redshift-matched sample of 102 *HST*-detected LAEs. $\text{Ly}\alpha$ is clearly detected with good agreement between the *HST*-detected/undetected LAEs, including the characteristic asymmetry of $\text{Ly}\alpha$.

Marino et al. 2018). While some narrowband studies have explicitly attempted to constrain the fraction of high-EW LAEs (Malhotra & Rhoads 2002; Gronwall et al. 2007; Ouchi et al. 2008; Zheng et al. 2014), detailed spectroscopic and photometric studies have only confirmed this picture in a few cases (e.g., Kashikawa et al. 2012; Hashimoto et al. 2017a).

Here we present a sample of 102 LAEs detected by MUSE that are not significantly detected in the *HST* imaging in the UDF, which reaches depths of 29.1–30.3 (Illingworth et al. 2013). We use spectral stacking (Section 2.1) and photometric stacking (Section 3) to confirm the MUSE $\text{Ly}\alpha$ redshifts and estimate the contamination fraction. Finally, we demonstrate that the observed fraction of *HST*-undetected LAEs is in line with theoretical expectations (Section 4). We adopt a flat Λ CDM cosmology ($\Omega_m = 0.3$, $\Omega_\Lambda = 0.7$, and $H_0 = 70 \text{ km s}^{-1} \text{Mpc}^{-1}$) and AB magnitudes (Oke 1974) throughout.

2. Data and Sample Selection

We utilize the MUSE spectroscopic data set in the UDF, covering 9.92 arcmin^2 to 10 hr depth and a single 1.15 arcmin^2 subfield to 32 hr depth; further details about the observations and data reduction are presented in B17.

The positioning of the MUSE data was designed to maximize the overlap with *HST* imaging in the UDF, the deepest imaging at UV, optical, and near-infrared wavelengths ever taken. Here, we utilize the reductions from Illingworth et al. (2013), who combine all epochs of imaging from all major surveys in the area (ACS *F435W*, *F606W*, *F775W*, and *F850LP*; WFC3/IR *F105W*, *F125W*, *F140W*, and *F160W*). We supplement these images with WFC3/UV *F225W* data (Teplitz et al. 2013) and *F275W* and *F336W* data (Oesch et al. 2018).

We use the 160 sources from B17 with flux-weighted emission line centroids that cannot be attributed to photometric objects in the Rafelski et al. (2015, hereafter R15) catalog within $0''.6$ (the FWHM of MUSE; see Section 3.1 of Inami et al. 2017, hereafter I17). These sources were identified via a spatially and spectrally coherent emission line from the MUSE data using the ORIGIN software (Bourguignon et al. 2012; Paris 2013; B17; D. Mary et al. 2018, in preparation). As with the full I17 catalog, redshifts are determined via template

cross-correlation and human inspection. Combined with the fact that $\text{Ly}\alpha$ is spectrally resolved in MUSE, this means that a majority of the LAEs have fluxes far above the nominal $3\text{-}\sigma$ limit (see Figure 1 and Table 1).

2.1. Detected versus Undetected

With this sample of 160 objects that are not in the R15 catalog, we proceed to measure the magnitudes in order to exclude all *HST*-detected objects. We utilize the signal-to-noise ratio (S/N) in *HST* images within a $0''.4$ aperture centered on the $\text{Ly}\alpha$ centroid from ORIGIN. This aperture corresponds to a physical size of 3.1 kpc (2.2 kpc) at $z = 2.9$ (6.6). However, as shown in Section 3, stacked images show that the objects are, on average, more compact than this aperture (and in agreement with measured size–luminosity relations, e.g., Shibuya et al. 2015).

The local background level is calculated by measuring the standard deviation of the fluxes in 250 identical apertures spread randomly within a $10'' \times 10''$ cutout centered on the object, with other objects masked according to the R15 segmentation maps. Because the UDF is not uniform in all photometric bands (specifically the WFC3 coverage), it is crucial to measure the *local* background level instead of relying on the average depth of the field. If the aperture flux is greater than five times the local background level in an *HST* band, then we consider the object “detected” in that band.

In total, we find that 102 of the ORIGIN sources are not detected above $5\text{-}\sigma$ in any of the *HST* imaging bands, all of which have redshifts classified as $\text{Ly}\alpha$ (I17). This represents 12.6% of the full I17 LAE sample. At $z > 6$ where an LAE has most of its flux redward of *F850LP*, we only have a single object that lies outside of the deepest WFC3/infrared data in the UDF.

Their $\text{Ly}\alpha$ fluxes and redshifts compared to the full MUSE sample of *HST*-detected LAEs are shown in the left panel of Figure 1. Compared to a $\text{Ly}\alpha$ flux- and redshift-matched sample of *HST*-detected MUSE LAEs, we see a similar $\text{Ly}\alpha$ amplitude and spectral profile (right panel of Figure 1; see I17 for details on the spectral extractions), confirming the reality of the ORIGIN line detections. The MUSE “*HST*-undetected” sample is presented in Table 1. The median aperture S/N in

Table 1
Properties of *HST*-undetected MUSE LAEs

MUSE ID (I17)	R.A. (deg)	Decl. (deg)	z	$\text{Ly}\alpha$ Flux ($\times 10^{-20}$ erg s $^{-1}$ cm $^{-2}$)	$\log \text{Ly}\alpha$ Luminosity (erg s $^{-1}$)	S/N $F435W$	S/N $F606W$	S/N $F775W$
6316	53.17032	-27.77835	4.446	153. \pm 7.94	41.48 \pm 0.02251	-1.1	-0.34	-1.0
6317	53.16767	-27.77743	5.404	277. \pm 13.6	41.94 \pm 0.02140	0.23	0.58	4.2
6318	53.16665	-27.77651	4.555	82.1 \pm 7.49	41.23 \pm 0.03963	-0.29	0.022	2.9
6320	53.16465	-27.78574	4.516	92.9 \pm 8.20	41.28 \pm 0.03831	-0.0024	1.6	3.6
6321	53.16334	-27.78037	3.765	139. \pm 13.1	41.27 \pm 0.04095	0.0049	2.7	2.7
6323	53.16276	-27.77056	3.499	212. \pm 14.7	41.37 \pm 0.03009	0.73	3.0	1.3
6325	53.16234	-27.78630	3.417	196. \pm 13.7	41.32 \pm 0.03041	0.051	4.4	2.6
6326	53.16227	-27.77738	5.919	230. \pm 9.18	41.95 \pm 0.01734	-0.68	-0.37	1.5
6327	53.16194	-27.77287	5.135	202. \pm 8.99	41.75 \pm 0.01929	0.24	0.46	1.0
6328	53.16179	-27.77750	4.777	74.4 \pm 6.56	41.24 \pm 0.03831	0.16	1.3	2.4
6329	53.16173	-27.77081	3.329	681. \pm 14.7	41.83 \pm 0.009403	0.075	-0.11	-0.66
6330	53.16055	-27.77892	3.749	136. \pm 11.4	41.25 \pm 0.03652	-0.25	1.8	1.6
6331	53.15845	-27.77810	5.530	134. \pm 10.2	41.65 \pm 0.03298	-0.19	0.32	3.2
6332	53.15814	-27.77848	6.335	194. \pm 19.0	41.94 \pm 0.04259	-0.28	-0.69	0.58
6333	53.15697	-27.78711	5.691	166. \pm 12.9	41.77 \pm 0.03384	-0.68	1.9	2.3
6334	53.15574	-27.78724	4.768	167. \pm 12.0	41.59 \pm 0.03127	0.32	1.7	3.8
6335	53.15513	-27.78330	4.370	113. \pm 10.1	41.33 \pm 0.03860	0.35	-0.054	0.66
6336	53.15480	-27.77305	3.715	220. \pm 12.4	41.45 \pm 0.02455	1.2	1.5	0.37
6337	53.15464	-27.77693	5.764	109. \pm 7.86	41.60 \pm 0.03125	-0.51	-0.73	0.24
6338	53.15436	-27.77192	3.338	202. \pm 13.3	41.30 \pm 0.02874	0.24	4.8	2.6
6339	53.15416	-27.78242	5.131	113. \pm 6.92	41.49 \pm 0.02665	-0.043	-0.85	3.7
6340	53.15334	-27.78133	4.510	104. \pm 8.95	41.33 \pm 0.03736	-0.16	0.85	2.8
6341	53.15254	-27.78379	4.777	231. \pm 6.40	41.73 \pm 0.01204	0.0042	3.0	4.7
6342	53.15206	-27.78131	4.514	172. \pm 11.3	41.55 \pm 0.02863	0.0098	1.0	1.2
6370	53.17894	-27.80160	4.840	135. \pm 15.5	41.51 \pm 0.05006	0.025	1.1	1.9
6371	53.16639	-27.79263	6.369	320. \pm 86.7	42.17 \pm 0.1176	-0.053	1.1	1.0
6373	53.14410	-27.78138	6.504	114. \pm 22.7	41.74 \pm 0.08648	-0.19	-0.089	1.4
6374	53.15889	-27.80813	3.177	202. \pm 27.3	41.25 \pm 0.05867	-0.15	-0.82	1.1
6375	53.14320	-27.78798	3.417	463. \pm 28.9	41.69 \pm 0.02713	-0.014	1.6	0.17
6376	53.16883	-27.79413	4.285	384. \pm 20.9	41.84 \pm 0.02364	0.20	4.4	4.1
6380	53.16261	-27.79550	5.453	218. \pm 31.6	41.84 \pm 0.06294	1.1	-0.22	2.8
6384	53.18069	-27.79774	6.369	316. \pm 70.2	42.16 \pm 0.09667	-0.078	-0.36	-1.4
6388	53.17152	-27.76599	3.000	347. \pm 33.8	41.43 \pm 0.04237	0.0098	-1.1	-0.75
6390	53.17702	-27.77742	3.836	291. \pm 25.1	41.61 \pm 0.03744	0.12	0.91	-0.88
6392	53.14792	-27.79069	4.472	134. \pm 15.7	41.43 \pm 0.05073	0.091	0.96	0.70
6394	53.18567	-27.79298	4.027	218. \pm 23.1	41.53 \pm 0.04617	0.0064	1.7	1.4
6395	53.14853	-27.76570	5.050	127. \pm 13.1	41.53 \pm 0.04487	-0.56	-1.0	3.9
6398	53.14905	-27.79529	5.627	117. \pm 27.5	41.60 \pm 0.1023	-0.42	-0.33	-0.20
6399	53.18019	-27.77279	3.195	241. \pm 28.4	41.34 \pm 0.05110	1.5	3.8	0.32
6402	53.17338	-27.79836	4.372	136. \pm 21.4	41.41 \pm 0.06850	-0.21	-0.31	-0.49
6404	53.14312	-27.77649	3.220	259. \pm 26.4	41.38 \pm 0.04425	0.17	-0.26	1.4
6405	53.13085	-27.78203	5.130	137. \pm 14.4	41.58 \pm 0.04578	-1.8	-1.9	2.0
6407	53.13436	-27.77980	4.178	377. \pm 22.7	41.81 \pm 0.02617	-1.3	2.1	2.9
6408	53.14776	-27.77261	4.270	210. \pm 19.4	41.58 \pm 0.04011	0.17	4.4	2.2
6414	53.16055	-27.81939	3.701	567. \pm 28.8	41.86 \pm 0.02204	0.20	-0.69	-2.0
6420	53.14606	-27.77609	4.265	277. \pm 18.4	41.70 \pm 0.02874	-0.13	0.90	2.9
6422	53.15154	-27.80465	4.574	131. \pm 14.7	41.44 \pm 0.04886	0.25	-0.53	1.4
6423	53.13403	-27.78150	5.781	297. \pm 21.1	42.04 \pm 0.03088	-0.093	-0.68	1.3
6425	53.17353	-27.80048	5.292	196. \pm 23.0	41.77 \pm 0.05078	-0.051	-0.36	1.2
6427	53.18823	-27.79075	4.824	348. \pm 14.9	41.92 \pm 0.01860	-0.012	2.4	4.3
6430	53.17782	-27.77873	3.987	196. \pm 19.0	41.48 \pm 0.04207	0.35	2.2	1.3
6432	53.16355	-27.77722	5.260	225. \pm 40.6	41.82 \pm 0.07827	0.67	-0.37	1.7
6433	53.16087	-27.80347	4.943	383. \pm 15.2	41.99 \pm 0.01718	-0.79	1.8	5.0
6434	53.14850	-27.78335	4.834	96.8 \pm 16.1	41.37 \pm 0.07230	0.64	1.4	4.8
6435	53.15718	-27.81387	5.050	501. \pm 32.3	42.13 \pm 0.02798	0.047	0.56	4.9
6436	53.14955	-27.77885	3.474	250. \pm 21.8	41.44 \pm 0.03775	-0.15	-0.48	-0.60
6442	53.13220	-27.78918	3.414	305. \pm 25.9	41.51 \pm 0.03687	0.10	3.0	2.7
6444	53.14823	-27.77638	5.133	189. \pm 16.6	41.72 \pm 0.03813	0.0063	0.70	2.7
6447	53.16890	-27.77583	4.810	205. \pm 14.5	41.69 \pm 0.03071	-1.3	1.2	2.9
6448	53.17235	-27.79514	4.764	179. \pm 20.1	41.62 \pm 0.04890	0.033	0.67	0.33
6451	53.16510	-27.81476	3.069	1980 \pm 34.9	42.21 \pm 0.007665	0.15	3.0	1.7
6453	53.13678	-27.79040	5.697	181. \pm 20.0	41.81 \pm 0.04799	0.44	1.9	3.3
6455	53.16598	-27.79315	5.322	169. \pm 16.6	41.71 \pm 0.04256	0.042	1.4	2.5

Table 1
(Continued)

MUSE ID (I17)	R.A. (deg)	Decl. (deg)	z	Ly α Flux ($\times 10^{-20}$ erg s $^{-1}$ cm $^{-2}$)	log Ly α Luminosity (erg s $^{-1}$)	S/N F435W	S/N F606W	S/N F775W
6457	53.13819	-27.79859	4.731	158. \pm 16.4	41.56 \pm 0.04519	-0.44	-0.67	1.5
6459	53.17243	-27.76556	3.432	727. \pm 26.7	41.89 \pm 0.01594	0.62	4.4	0.57
6472	53.14920	-27.80258	3.662	239. \pm 30.4	41.47 \pm 0.05536	-0.016	1.6	3.4
6473	53.16708	-27.78810	4.552	167. \pm 16.5	41.54 \pm 0.04305	-0.10	0.73	-0.0068
6477	53.17875	-27.79394	5.146	208. \pm 25.0	41.76 \pm 0.05219	0.76	1.3	4.3
6482	53.17760	-27.76991	4.512	208. \pm 18.3	41.63 \pm 0.03819	-0.46	1.5	2.6
6483	53.16077	-27.76837	4.306	215. \pm 17.1	41.60 \pm 0.03447	-0.0075	2.8	2.7
6487	53.16464	-27.80061	4.365	154. \pm 15.7	41.46 \pm 0.04438	-0.025	3.2	1.7
6488	53.16477	-27.76527	3.194	566. \pm 32.9	41.71 \pm 0.02526	0.41	0.34	0.36
6492	53.15175	-27.79985	3.974	370. \pm 22.7	41.75 \pm 0.02671	0.13	4.7	2.9
6495	53.15919	-27.81769	5.292	285. \pm 21.3	41.93 \pm 0.03248	-0.87	0.098	2.4
6496	53.17874	-27.80008	4.760	140. \pm 15.1	41.51 \pm 0.04671	0.19	0.32	2.6
6498	53.19483	-27.78460	4.542	500. \pm 16.9	42.02 \pm 0.01467	0.028	4.6	2.6
6499	53.15037	-27.77300	4.507	113. \pm 21.2	41.36 \pm 0.08126	-0.038	1.5	-0.11
6500	53.14859	-27.80947	3.153	208. \pm 29.2	41.26 \pm 0.06097	0.48	-1.5	1.8
6501	53.14731	-27.80701	5.315	221. \pm 17.7	41.82 \pm 0.03475	-0.45	-0.80	2.1
6502	53.15557	-27.76549	4.517	186. \pm 15.0	41.58 \pm 0.03519	-0.90	3.2	1.9
6505	53.14331	-27.79594	6.574	159. \pm 27.9	41.89 \pm 0.07614	0.20	0.20	-0.13
6507	53.17981	-27.79420	5.145	261. \pm 20.2	41.86 \pm 0.03372	0.17	0.68	3.3
6510	53.15479	-27.79515	4.135	252. \pm 25.8	41.62 \pm 0.04444	-0.52	3.7	0.72
6514	53.16816	-27.81561	3.257	271. \pm 75.1	41.41 \pm 0.1201	0.47	4.3	1.4
6517	53.17288	-27.77023	3.432	317. \pm 24.8	41.53 \pm 0.03396	0.19	1.5	-0.69
6520	53.16195	-27.76587	5.134	139. \pm 15.7	41.59 \pm 0.04914	0.13	1.4	2.5
6521	53.17383	-27.80033	3.069	327. \pm 30.5	41.43 \pm 0.04058	-0.032	1.5	0.25
6522	53.17494	-27.80086	3.565	227. \pm 28.8	41.42 \pm 0.05513	0.17	3.6	4.2
6524	53.15821	-27.76769	6.245	172. \pm 15.9	41.88 \pm 0.04000	-0.18	-0.48	-0.74
6525	53.13807	-27.77947	4.443	115. \pm 13.9	41.36 \pm 0.05241	0.86	3.8	1.8
6526	53.18049	-27.80063	5.782	217. \pm 18.3	41.90 \pm 0.03672	-0.0043	-0.29	4.1
6527	53.14812	-27.80685	3.171	292. \pm 33.2	41.41 \pm 0.04932	0.67	3.9	2.7
6528	53.14351	-27.77222	4.032	198. \pm 18.4	41.49 \pm 0.04035	-0.042	5.0	2.9
6533	53.17269	-27.77705	4.889	154. \pm 17.7	41.58 \pm 0.05004	-0.091	0.11	2.1
6534	53.13873	-27.78211	5.070	271. \pm 14.0	41.86 \pm 0.02251	-0.24	-0.13	4.8
6536	53.14850	-27.77441	2.949	471. \pm 39.7	41.54 \pm 0.03656	-0.087	-1.2	-0.47
6862	53.18553	-27.78331	3.565	357. \pm 28.1	41.62 \pm 0.03412	-0.051	3.8	1.6
6863	53.15368	-27.79120	3.608	95.0 \pm 25.4	41.06 \pm 0.1161	0.025	0.43	0.37
7392	53.14808	-27.79749	4.784	173. \pm 14.5	41.61 \pm 0.03631	0.0061	1.8	4.1
7393	53.17392	-27.78929	6.396	262. \pm 51.2	42.08 \pm 0.08483	0.82	-0.063	-0.33
7394	53.13801	-27.78969	3.606	333. \pm 22.5	41.60 \pm 0.02942	-0.13	1.5	0.74
7395	53.18794	-27.77833	3.007	230. \pm 32.3	41.25 \pm 0.06090	0.062	2.6	1.6

(This table is available in machine-readable form.)

F606W of our sample is 1.0, compared with 9.9 for the 663 MUSE-confirmed LAEs that are in the R15 catalog.

Of the 58 ORIGIN-only LAEs with an *HST* detection, 11 are detected only in the photometric band(s) that contains Ly α . While they are omitted from this sample, they are also plausibly high-EW LAEs because their UV continuum is still undetected (M. V. Maseda et al. 2018, in preparation). The remaining sources are not in the R15 catalog primarily because of their projected proximity to brighter galaxies (B17). Our sample is clearly separated from the *HST*-detected R15 sources at these redshifts, even though our aperture measurements often represent lower limits to the actual magnitudes (Figure 2).

3. *HST* Imaging Stacks

We create stacks in each imaging band, adopting three redshift bins ($2.974 < z < 4.646$, $4.877 < z < 5.678$, and $6.067 < z < 6.389$) spaced such that the Ly α flux lies in a

single *HST* band (F606W, F775W, and F850LP, respectively; see Figure 1). These bins contain 54, 22, and 4 objects.

In each bin we combine the *HST* imaging for all objects on a filter-by-filter basis. In each filter stack, we take the mean flux value at each pixel position, using the R15 segmentation maps to mask other sources. These stacks are shown in Figure 3, restricting the view to the band containing Ly α and the bands immediately redward/blueward. The UV continuum appears compact compared to the photometric aperture, and therefore we conclude that a majority of our sample have small sizes ($r_e \lesssim 1.5$ kpc). In addition, when combining all of the filters redward of Ly α for *individual* galaxies, 18 have a detection of their UV continuum. In these cases we do not measure a significant offset between the centroid of Ly α and the UV continuum (median $0''.09$, equal to the size of the *HST*/Advanced Camera for Surveys (ACS) point-spread function; compare Finkelstein et al. 2011; Sobral et al. 2017).

We perform aperture photometry on the stacks in the same way as described in Section 2.1. The UV continuum

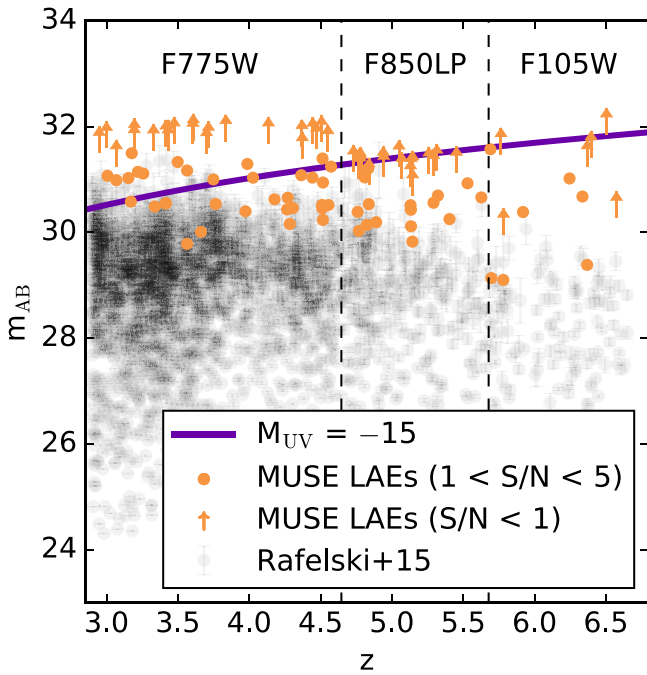


Figure 2. Redshift vs. observed magnitude for the 102 MUSE *HST*-undetected LAEs and the photometric sample of R15. Magnitudes are given in the band immediately redward of Ly α ; for the MUSE objects, the measurement is within a $0''.4$ aperture, with circles showing measurements ($S/N < 5$) and arrows showing the $1\text{-}\sigma$ noise level in the aperture when $S/N < 1$. The R15 redshifts are photometric whereas the MUSE redshifts are spectroscopic. A line of constant $M_{UV} = -15$ is shown in purple, similar to the values from stacks presented in Section 3. The MUSE sample is, by construction, much fainter than the R15 sample.

magnitudes, in the band redward of Ly α , for the two lower- z bins are -14.67 and -15.36 , and -15.37 ($1\text{-}\sigma$) for the highest- z bin, at the median redshifts within the bins.

The effect of Ly α on the two lower- z stacks is clear, resulting in strong detections in those bands. While undetected individually in F850LP and F105W, the high- z stack of four objects has a significance of $3.0\text{-}\sigma$ when the two filters are combined. The lack of detections in the blue bands indicates a drop in the spectral energy distribution, likely from the 1216 \AA break, further demonstrated by the fact that these stacks satisfy the color selections for “dropout” galaxies from Bouwens et al. (2015). This all implies that the average galaxy in our sample is indeed at the redshift expected based on the position and identification of Ly α .

If we were to use only the faintest objects in the sample (i.e., $S/N < 3$ in all *HST* bands), then we would have stacks of 30, 11, and 4 objects resulting in M_{UV} values of -14.07 , -15.29 , and -15.37 , also satisfying the “dropout” color selections.

3.1. Fraction of Interlopers

The primary source of contamination in our ORIGIN sample are emission lines being misidentified as Ly α . Ly α is often, but not always, identified via its characteristic asymmetry, otherwise a single emission feature is identified as Ly α when no other emission/absorption features can be detected in the spectrum. [O II] would be the primary line that is misidentified as Ly α , considering that other strong optical emission lines (H α , [O III], or H β) are almost never observed alone at MUSE wavelengths and [O II] is the only strong emission line observable at $0.9 < z < 1.5$. We expect misidentifications

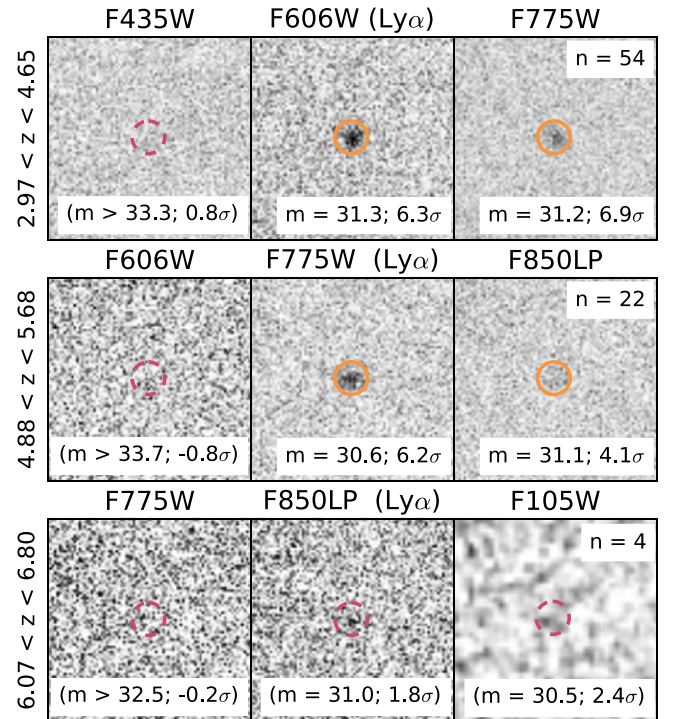


Figure 3. *HST* image stacks for the *HST*-undetected LAEs, separated into redshift bins. Each image is $2''.5$ on a side; the solid (dashed) circle shows a $0''.4$ aperture with $>3\text{-}\sigma$ detections (non-detections) in orange (pink). The 1216 \AA break is demonstrated by non-detections in the left panels as well as Ly α emission and the UV continuum in the central/right panels, providing photometric proof that the average object is a high- z LAE. Numbers of objects per stack, magnitudes ($1\text{-}\sigma$ limits when $S/N < 1$), and detection significances are also shown.

predominantly at low S/N , as the spectral resolution of MUSE is high enough to differentiate the two peaks of the [O II] doublet ($\approx 200\text{ km s}^{-1}$) from the typical separation of double-peaked $z \approx 3\text{--}6$ LAEs ($\approx 500\text{ km s}^{-1}$; Trainor et al. 2015; Verhamme et al. 2018).

In order to assess the potential contamination fraction we recreate the *HST* imaging stacks shown in Figure 3, randomly replacing a number of the (plausible) LAEs, n , with MUSE-confirmed [O II] emitters with a similar line flux and line position. For these “contaminated” samples with varying n we perform the same stacking procedure, measuring the S/N in the band blueward of (the misidentified) Ly α (F435W, F606W, and F775W, respectively) which is critical in identifying the 1216 \AA break. This procedure is repeated 1000 times (replacing a random subset of n objects with [O II] emitters each time) to measure the fraction of cases where the stacks are detected at $>3\text{-}\sigma$. For these stacks, $n \geq 3$, 1, and 1 produces detections in the blue band $>99.7\%$ of the time, implying contamination fractions of $<6\%$, $<5\%$, and $<25\%$, respectively.

4. Comparison to Continuum-detected Samples

In order to assess whether the *HST*-undetected objects are a separate population or an extension of the *HST*-detected population, we construct an empirical model based on a distribution of rest-frame Ly α EWs and a distribution of UV continuum magnitudes. We use the observed EW distribution for *HST*-detected MUSE LAEs in the UDF (Hashimoto et al. 2017b), assuming no evolution in this distribution with redshift or $L_{Ly\alpha}$ (see their Section 6.3). The best-fit lognormal

distribution has a mean EW of 119 Å (15% of objects have EWs in excess of 200 Å). We model the distribution of M_{UV} values as a power law with α -slopes from Bouwens et al. (2015) at $z \sim 4$, 5, and 6.

By combining these distributions, we can predict the number of objects with a given M_{UV} and $EW_{Ly\alpha}$. These two parameters determine the number of objects that would be spectroscopically detectable by MUSE with total luminosities (line plus continuum) that would have been observed at the average depth of the *HST* imaging: 30.1 in *F606W*, 30.1 in *F775W*, and 29.2 in *F850LP*, depending on the redshift (Illingworth et al. 2013), and including the mean attenuation of the intergalactic medium (Inoue et al. 2014). This model can be inverted for a given $L_{Ly\alpha}$ to give the number of sources above the *HST* limits (for the assumed EW distribution). We use larger redshift ranges ($2.9 < z < 4.88$, $4.88 < z < 6.07$, and $6.07 < z < 6.65$) than in Section 3 as the contribution of $Ly\alpha$ to a bluer/redder *HST* band is not important. The resulting predictions for the undetected fraction as a function of $L_{Ly\alpha}$ are shown in Figure 4, using the observed redshift distribution of the MUSE *HST*-undetected sources. Overplotted is the fraction of *HST*-detected/undetected sources from MUSE.

Overall, this model accurately reproduces the observed fractions: comparing the distributions of $L_{Ly\alpha}$, we obtain p -values from a Kolmogorov–Smirnov test of 0.07, 0.68, and 0.97. While this does not imply with certainty that this is the *best* model to explain the observations, it means that the *HST*-undetected LAEs are consistent with being the (high-EW) tail of the distribution of *HST*-detected LAEs.

A natural question is whether the phenomenon of a MUSE line detection without an *HST* counterpart occurs for emission lines other than $Ly\alpha$. For example, there are no cases where ORIGIN detects [O II] emission without an *HST* counterpart. We can perform a similar analysis to the one above to see if this matches expectations. We adopt the [O II] luminosity function from Pirzkal et al. (2013), measured from *HST*/ACS slitless grism spectroscopy with coverage of [O II] from $0.9 < z < 1.5$, which is the high- z range probed by MUSE. At the luminosities probed by MUSE, this function can be approximated by a power law with a slope $\alpha = -1.93$. This is combined with the EW distribution from Pirzkal et al. (2013) (or I17) to estimate the continuum levels. We predict that the incidence of *HST*-undetected [O II] emission is essentially zero for $L_{[O II]} > 10^{39.5} \text{ erg s}^{-1}$ ($6 \times 10^{-19} \text{ erg s}^{-1} \text{ cm}^{-2}$ at $z = 1$). Only at $m_{F606W} = 29.2$ (0.9 magnitudes brighter than our data) would we expect 10% of $z = 1$ [O II] emitters at this luminosity to remain undetected in the continuum.

5. Discussion and Conclusions

We have discussed a sample of 102 emission line sources discovered with ultra-deep MUSE spectroscopy in the UDF. While they are all individually below the detection limits in *HST*-based imaging, stacks show flux distributions that are expected if these emission lines are predominantly $Ly\alpha$. Notably, a strong detection in the *HST* bands expected to contain $Ly\alpha$ and the UV continuum from the two well-populated stacks at $2.974 < z < 4.646$ and $4.877 < z < 5.678$, and in stacked MUSE spectra, implies that the ORIGIN line detections are robust. A detection in the combined $Ly\alpha$ and

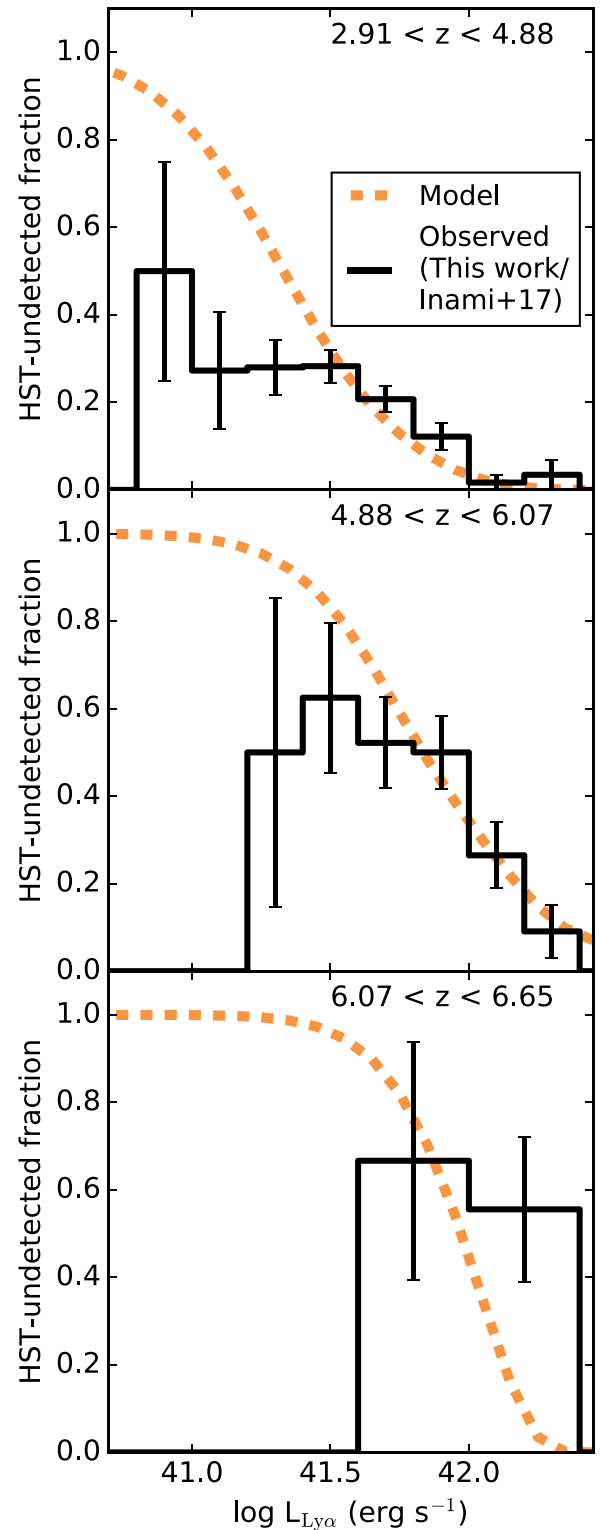


Figure 4. Observed (histogram; Poisson errors) and predicted (dashed line) fraction of LAEs in a MUSE-selected sample ($f_{Ly\alpha} > 3 \times 10^{-19} \text{ erg s}^{-1} \text{ cm}^{-2}$) that are undetected in broadband imaging at the depth of the UDF. The model is based on UV luminosity functions (Bouwens et al. 2015) and a $Ly\alpha$ EW distribution (Hashimoto et al. 2017b). Using the observed redshift distribution of undetected sources, the model predicts the dashed curve. Without any additional tuning we observe good agreement between the prediction and the observed fractions at all redshifts, implying that the *HST*-detected and undetected objects follow similar trends in UV magnitude and rest-frame $Ly\alpha$ EW.












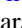

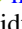

UV-continuum image in the $6.067 < z < 6.389$ bin also hints at the same conclusion. We have quantified the amount of contamination from [O II] emission lines that are misidentified as Ly α and find that the observed spectral break would disappear for contamination fractions as low as 5%. Finally, a simple model utilizing UV luminosity functions and an empirical Ly α EW distribution can reproduce the observed fraction of *HST*-undetected LAEs in our MUSE sample, implying that these sources are consistent with being an extension of the general population of LAEs.

Our stacking experiment reveals $M_{UV} \sim -15$ for these LAEs, or even -14 for the faintest subset. Compared to spectroscopically confirmed narrowband LAEs (e.g., Ouchi et al. 2008; Kashikawa et al. 2011; Zheng et al. 2014, $M_{UV} \gtrsim -17.5$), Lyman-break galaxies (e.g., Stark et al. 2010, $M_{UV} \gtrsim -18$), or MUSE LAEs in the UDF with *HST* counterparts (Hashimoto et al. 2017b, $M_{UV} \lesssim -16$), this sample is considerably fainter and represents the faintest objects at these redshifts with spectroscopic confirmations. These magnitudes are comparable to those of local blue compact dwarfs such as I Zw 18 ($M_{UV} = -14.7$; Gil de Paz et al. 2007). An abundant population of galaxies with such faint magnitudes at $z > 6$ are thought to be required in order to reionize the universe (Bouwens et al. 2012; Finkelstein et al. 2012), yet even our highly sensitive observations confirm $< 1\%$ of the expected numbers at $5 < z < 6.7$ with $-16 < M_{UV} < -14$ based on the $z \sim 6$ luminosity function (Bouwens et al. 2015), presumably those with the highest-EWs.

The ability to find emission lines in such faint sources crucially hinges on both the depth of the imaging data (to confirm the faint continua) as well as the depth of the spectroscopic data (these MUSE data probe line fluxes up to $10\times$ fainter than narrowband studies at similar redshifts: Drake et al. 2017; Hashimoto et al. 2017b; Karman et al. 2017), which is unique to the MUSE UDF Survey. The next step is to properly characterize the physical properties of this unique population. By pushing toward LAEs with higher EWs, we can push toward the lowest ages (and hence masses) and metallicities. While this is challenging with traditional studies (Hashimoto et al. 2017a), we can perform robust statistical measurements using the MUSE spectroscopic sample due to the stringent constraints provided by the *HST* imaging.

R.B. acknowledges support from ERC grant 339659-MUSICOS. J.B. is supported through Investigador FCT contract IF/01654/2014/CP1215/CT0003, national funds (UID/FIS/04434/2013), and by FEDER through COMPETE2020 (POCI-01-0145-FEDER-007672). J.S. acknowledges support from ERC grant 278594-GasAroundGalaxies. S.C. acknowledges support from Swiss National Science Foundation grant PP00P2_163824. T.C. and N.B. acknowledge support from ANR FOGHAR (ANR-13-BS05-0010-02), OCEVU Labex (ANR-11-LABX-0060), and the A*MIDEX project (ANR-11-IDEX-0001-02) funded by the “Investissements d’avenir” program managed by the ANR. J.R. acknowledges support from ERC grant 336736-CALENDS. A.V. acknowledges support from ERC grant 757258-TRIPLE.

ORCID iDs

Michael V. Maseda  <https://orcid.org/0000-0003-0695-4414>
 Marijn Franx  <https://orcid.org/0000-0002-8871-3026>
 Jarle Brinchmann  <https://orcid.org/0000-0003-4359-8797>
 Joop Schaye  <https://orcid.org/0000-0002-0668-5560>
 Leindert A. Boogaard  <https://orcid.org/0000-0002-3952-8588>
 Nicolas Bouché  <https://orcid.org/0000-0003-0068-9920>
 Rychard J. Bouwens  <https://orcid.org/0000-0002-4989-2471>
 Thierry Contini  <https://orcid.org/0000-0003-0275-938X>
 Takuya Hashimoto  <https://orcid.org/0000-0002-0898-4038>
 Raffaella A. Marino  <https://orcid.org/0000-0002-8559-6565>
 Sowgat Muzahid  <https://orcid.org/0000-0003-3938-8762>
 Themiya Nanayakkara  <https://orcid.org/0000-0003-2804-0648>
 Johan Richard  <https://orcid.org/0000-0001-5492-1049>
 Kasper B. Schmidt  <https://orcid.org/0000-0002-3418-7251>
 Anne Verhamme  <https://orcid.org/0000-0002-2201-1865>

References

- Bacon, R., Accardo, M., Adjali, L., et al. 2010, Proc. SPIE, 7735, 773508
 Bacon, R., Brinchmann, J., Richard, J., et al. 2015, *A&A*, 575, A75
 Bacon, R., Conseil, S., Mary, D., et al. 2017, *A&A*, 608, A1
 Bourguignon, S., Mary, D., & Slezak, E. 2012, *StMet*, 9, 32
 Bouwens, R. J., Illingworth, G. D., Oesch, P. A., et al. 2012, *ApJL*, 752, L5
 Bouwens, R. J., Illingworth, G. D., Oesch, P. A., et al. 2015, *ApJ*, 803, 34
 Charlot, S., & Fall, S. M. 1993, *ApJ*, 415, 580
 Drake, A. B., Garel, T., Wisotzki, L., et al. 2017, *A&A*, 608, A6
 Finkelstein, S. L., Cohen, S. H., Windhorst, R. A., et al. 2011, *ApJ*, 735, 5
 Finkelstein, S. L., Papovich, C., Ryan, R. E., et al. 2012, *ApJ*, 758, 93
 Gil de Paz, A., Boissier, S., Madore, B. F., et al. 2007, *ApJS*, 173, 185
 Gronwall, C., Ciardullo, R., Hickey, T., et al. 2007, *ApJ*, 667, 79
 Hashimoto, T., Garel, T., Guiderdoni, B., et al. 2017b, *A&A*, 608, A10
 Hashimoto, T., Ouchi, M., Shimasaku, K., et al. 2017a, *MNRAS*, 465, 1543
 Illingworth, G. D., Magee, D., Oesch, P. A., et al. 2013, *ApJS*, 209, 6
 Inami, H., Bacon, R., Brinchmann, J., et al. 2017, *A&A*, 608, A2
 Inoue, A. K., Shimizu, I., Iwata, I., & Tanaka, M. 2014, *MNRAS*, 442, 1805
 Karman, W., Caputi, K. I., Caminha, G. B., et al. 2017, *A&A*, 599, A28
 Kashikawa, N., Nagao, T., Toshikawa, J., et al. 2012, *ApJ*, 761, 85
 Kashikawa, N., Shimasaku, K., Matsuda, Y., et al. 2011, *ApJ*, 734, 119
 Malhotra, S., & Rhoads, J. E. 2002, *ApJL*, 565, L71
 Marino, R. A., Cantalupo, S., Lilly, S. J., et al. 2018, *ApJ*, 859, 53
 Maseda, M. V., van der Wel, A., Rix, H.-W., et al. 2018, *ApJ*, 854, 29
 Oesch, P. A., Montes, M., Reddy, N., et al. 2018, *ApJS*, 237, 12
 Oke, J. B. 1974, *ApJS*, 27, 21
 Ouchi, M., Shimasaku, K., Akiyama, M., et al. 2008, *ApJS*, 176, 301
 Paris, S. 2013, Theses, Université Nice Sophia Antipolis, Università degli studi La Sapienza, <https://tel.archives-ouvertes.fr/tel-00933827>
 Pirzkal, N., Rothberg, B., Ly, C., et al. 2013, *ApJ*, 772, 48
 Rafelski, M., Teplitz, H. I., Gardner, J. P., et al. 2015, *AJ*, 150, 31
 Raiter, A., Schaerer, D., & Fosbury, R. A. E. 2010, *A&A*, 523, A64
 Schaerer, D. 2003, *A&A*, 397, 527
 Shibuya, T., Ouchi, M., & Harikane, Y. 2015, *ApJS*, 219, 15
 Sobral, D., Matthee, J., Best, P., et al. 2017, *MNRAS*, 466, 1242
 Stark, D. P., Ellis, R. S., Chiu, K., Ouchi, M., & Bunker, A. 2010, *MNRAS*, 408, 1628
 Teplitz, H. I., Rafelski, M., Kurczynski, P., et al. 2013, *AJ*, 146, 159
 Trainor, R. F., Steidel, C. C., Strom, A. L., & Rudie, G. C. 2015, *ApJ*, 809, 89
 Verhamme, A., Garel, T., Ventou, E., et al. 2018, *MNRAS*, 478, L60
 Zheng, Z.-Y., Wang, J.-X., Malhotra, S., et al. 2014, *MNRAS*, 439, 1101